



One-pot synthesis of composite NiO/graphitic carbon flakes with contact glow discharge electrolysis for electrochemical supercapacitors

Anis Allagui^{1,*†}, Tareq Salameh¹ and Hussain Alawadhi²

¹Department of Sustainable and Renewable Energy Engineering, University of Sharjah, PO Box 27272, Sharjah, UAE

²Department of Applied Physics, University of Sharjah, PO Box 27272, Sharjah, UAE

SUMMARY

Thanks to their high power density and degree of reversibility, supercapacitors are electrochemical devices that narrow the gap between secondary batteries and traditional dielectric capacitors in the traditional Ragone plot. However, their use is still hindered by their capability to achieve higher energy density. In this work, we present a one-pot synthesis procedure of composite graphitic carbon flake-supported NiO for electrochemical energy storage application. We used cathodic contact glow discharge electrolysis by applying 120 Vdc terminal voltage between a thin Pt wire, slightly submerged in an aqueous solution of $\text{NiSO}_4(\text{H}_2\text{O})_6 + \text{Na}_2\text{SO}_4$, and a large surface area carbon graphite anode. Strong active species generated within the micro-plasma volume locally reduce the nickel precursors to form NiO materials, while at the anodically polarized graphite rod, the forces holding the graphene layers together are weakened by ion/solvent intercalation producing micrometer-sized graphitic carbon flakes. The morphological characterization is carried out by electron microscopy, energy dispersive X-ray spectroscopy, powder X-ray diffraction, and micro-Raman spectroscopy. Cyclic voltammetry, constant-current charge/discharge, and electrochemical impedance spectroscopy in 5 mol l⁻¹ KOH solution are carried out to evaluate the electrochemical energy storage performance of the material. We show that carbon flake-supported NiO exhibits the dual combination of electric double-layer capacitance with faradic behavior, giving 495 F g⁻¹ specific capacitance at 2 A g⁻¹ current density. Copyright © 2015 John Wiley & Sons, Ltd.

KEY WORDS

glow discharge electrolysis; graphite; nickel oxide; composite

Correspondence

*Anis Allagui, Department of Sustainable and Renewable Energy Engineering, University of Sharjah, PO Box 27272, Sharjah, UAE.

†E-mail: aallagui@sharjah.ac.ae

Received 9 April 2015; Revised 11 June 2015; Accepted 14 July 2015

1. INTRODUCTION

The continuous depletion of conventional resources of energy and the ever-increasing environmental awareness led to a soaring race for the development of energy conversion/storage alternatives. Many methods of energy storage are available, including batteries, supercapacitors, flywheels, compressed air, hydraulics, and superconducting magnetic energy storage systems. Supercapacitors stand out among these technologies; they are maintenance free and operate safely at ambient temperatures while exhibiting high power density, high specific capacitance, and excellent cyclability, inasmuch as they have attracted tremendous research activity over the past few years. Thanks to their high power exchange capability compared with batteries, supercapacitor energy storage systems have found use, for example, in grid stabilization applications, where they are interfaced to static synchronous

compensators [1], and in hybrid electric vehicles, where they are coupled with fuel cells to reduce their dynamic loading limitation [2].

A number of materials have been tested and used for electrochemical energy storage applications, including activated graphite, carbon nanotubes, carbon films, carbon foams, and graphene [3–8], which store the electrical energy by ion absorption in the electrical double layer. Carbon-based materials are among the top candidates owing to their easy and cost-effective manufacturing, along with tunable morphology and porosity, electrochemical inertness, high electric conductivity, and nontoxicity. Furthermore, some electronically conducting polymers, such as polyaniline, poly(pyrrole), polythiophene, poly(3-methylthiophene), and poly(3,4-ethylenedioxythiophene) [9–12], and nanostructured transition metal oxides, such as RuO_2 , IrO_2 , NiO_x , MnO_x , CoO_x , and CuO [13–19], can store energy pseudocapacitively or by fast and

reversible faradic redox reactions. This leads to both high capacitance values and larger range for the operating cell voltage [3]. Although a considerable amount of work has been dedicated to find supercapacitor materials with high electrochemical performance, the most studied options are usually large band gap semiconductors and sometimes insulators with poor electric conductivity [13]. As a result, dissipation of excess energy with charge/discharge cycles into Joule heating may make the electrochemical device unstable. The alternative is to form composite materials of pseudocapacitive transition metal oxides with conductive carbonaceous additives [20–23].

NiO is a material of choice for supercapacitor applications as a result of its high theoretical capacitance estimated to be 2583 F g^{-1} ($c = F/M\Delta V$ where F is the Faraday's constant, $\Delta V \approx 0.5 \text{ V}$ the operating voltage, and M the molar mass) in alkaline solution, assuming one OH^- per one NiO molecule. Additionally, it is widely available, relatively inexpensive, known for its high chemical and thermal stability, and easily engineered in many microstructured and nanostructured forms [21,24–29]. Herein, we report a facile single-step synthesis process of NiO materials on graphitic carbon flakes support using nonthermal contact glow discharge electrolysis (CGDE). It has been previously reported on the use of cathodic CGDE for the synthesis of NiO nanomaterials [15,30,31], which relies on the strong reducing species present in the micro-plasma volume surrounding the cathodically polarized electrode. By using a carbon graphite anode, we demonstrate that the final product is composed of NiO in addition to graphitic carbon flakes of large lateral size. This results from the weakening of forces holding the graphene layers together by volume expansion and electrochemical exfoliation of the carbon anode. The morphological characterization of the composite material is carried out by scanning electron microscopy (SEM) equipped with energy-dispersive X-ray spectrometer (EDX), powder X-ray diffraction (XRD), and micro-Raman spectroscopy. The electrochemical measurements are conducted using cyclic voltammetry (CV), galvanostatic charge/discharge, and electrochemical impedance spectroscopy (EIS) techniques in 5 mol l^{-1} KOH and show that the obtained material exhibits the combined effects of electric double-layer capacitance of graphitic carbon, with the electrochemical behavior of NiO.

2. EXPERIMENTAL

2.1. Synthesis of composite NiO/graphitic carbon flakes

The microstructured material has been synthesized with cathodic CGDE, as shown in Figure 1. The setup consists of a 75 ml aqueous solution of 0.3 mol l^{-1} $\text{NiSO}_4(\text{H}_2\text{O})_6$ and 0.5 mol l^{-1} Na_2SO_4 under gentle and continuous stirring. A platinum wire (0.5 mm diameter, 99.99% purity), immersed ca. 3 mm into the solution served as the cathode,

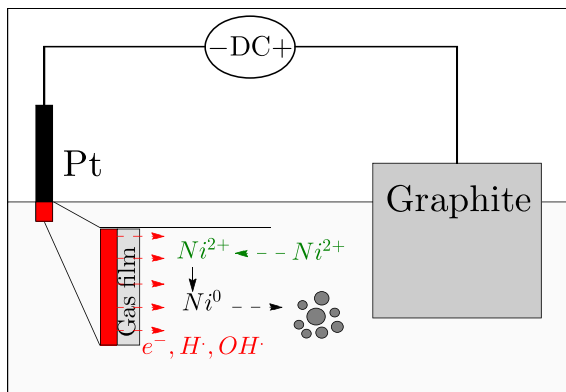


Figure 1. Setup of cathodic contact glow discharge electrolysis used for the synthesis of composite NiO-graphitic flakes material. Ni^{2+} precursors are locally reduced by strong reducing agents generated in the micro-plasma volume covering the Pt cathode, while the carbon graphite anode is exfoliated by ion/solvent intercalation and volume expansion.

and a graphite rod of 6 mm diameter immersed up to 5 cm served as an anode. The applied voltage was set to 120 Vdc for 90 min provided by a programmable Sorensen (Ametek) XG 300-5 power supply. The current fluctuated between ca. 200 and 300 mA [32]. The obtained material was extracted by a series of centrifugation (6000 rpm – 10 min) and cleaning cycles with deionized water. Subsequently, it was left to dry for 12 h at 60°C and stored in water for further characterization.

2.2. Physicochemical characterization

Electron microscopy and elemental analysis of the obtained composite material deposited on Si substrate was carried out using a VEGA3 XM (TESCAN) SEM equipped with EDX detector. The powder XRD patterns for crystal identification were recorded in the 2θ geometry between 20° and 70° at 0.02° 2θ step size with a Bruker D8 Advance DaVinci multipurpose X-ray diffractometer (Cu $\text{K}\alpha$ radiation; $\lambda = 1.5406 \text{ \AA}$). The Raman spectra were measured at room temperature in the back scattering configuration with a Renishaw InVia Raman microscope, with 514 nm excitation Ar ion laser on ca. $1 \mu\text{m}^2$ illumination spot. The sample was deposited on a clean microscope slide.

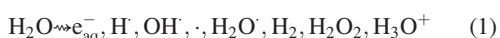
2.3. Electrochemical characterization

The potentiodynamic and constant-current charge/discharge measurements were conducted at room temperature using a BioLogic VSP-300 electrochemical workstation in 5 mol l^{-1} KOH solution. The working electrode was prepared by depositing onto the cross section of a polished 6 mm diameter graphite rod a mixture of the composite NiO/graphitic flakes with polytetrafluoroethylene binder at the mass ratios 96.67% to 3.33%. The active material loading was ca. 0.35 mg cm^{-2} . A Pt wire served as a counter electrode and a saturated standard calomel

(SCE) electrode as reference. EIS was conducted at open-circuit potential with a 10 mV amplitude sinusoidal signal between $f=500$ kHz down and 50 mHz using 20 points per decade.

3. RESULTS AND DISCUSSION

The synthesis mechanism of composite graphitic carbon flake-supported NiO material is attributed to the electrochemistry at both cathode and anode interfaces with the electrolyte. Under the applied 120 Vdc terminal voltage, a nonthermal micro-plasma discharge is generated at the cathodic side of the cell, as the voltage drop is being shifted to it by using a much smaller submerged surface area compared with the anode. Water molecules undergo a series of reactions of dissociation, recombination, dimerization, and solvation giving elements not found under equilibrium or close-to-equilibrium conditions [30,31,33]:



Nickel precursors (Ni^{2+}) present in the solution are then progressively reduced while in the vicinity of the micro-plasma volume by strong reducing agents, such as e_{aq}^- and H^+ , while competing with the back reactions of oxidation with OH^- and O_2^- radicals, to name a few [15,30,31]. Eventually, the initially formed nickel-based atoms grow into nano/micro-sized aggregates of nickel and/or nickel oxides [30,34,31]. Furthermore, from the beginning of the synthesis process, we observed a progressive dissociation of the graphite anode and its dispersion in the solution. Because in the sp^2 -hybridized carbon graphite the fourth electron lies in a $\text{p}\pi$ -orbital forming a weak π -bond with a π -orbital on neighboring atom, anions/solvent intercalation peels off layers of the graphitic anode by volume expansion [35,36]. Therefore, the obtained mixture is the result of Ni^{2+} reduction in the micro-plasma volume with graphitic carbon flakes resulting from the exfoliation of the anode. This is confirmed by the SEM micrograph and corresponding C, Ni, and O EDX mapping shown in Figure 2. We observe carbon flakes of irregular shapes in the tens of microns lateral size, mixed with micro-sized to nano-sized NiO particles, as shown from the superposition of Ni and O EDX maps [34]. The average mass ratio of carbon to NiO is found to be ca. 6.7 times from EDX

analysis. This is probably due the surface area ratio as well as the different kinetics of reactions at both cathodic and anodic interfaces with the solution. Compared with other chemical and electrochemical synthesis techniques, CGDE has the merit of combining two (or more) reaction sites of low and high current densities, which can be beneficial for both processing time and versatility.

The obtained material has been characterized by powder XRD, as shown in Figure 3, where both carbon graphite and NiO diffraction lines are identified. A relatively intense, narrow, and symmetric diffraction response is centered at 26.55° and attributed to graphite (002) indicating a highly ordered graphitic carbon structure. We can also see the diffraction lines at Bragg angles 42.46° , 44.50° , and 54.57° for the respective (hkl) Miller indices (100), (101), and (004) of graphite (ICDD PDF 00-056-0159). The crystalline phase of fcc NiO is identified from the 2θ angles 37.28° , 43.32° , and 62.90° corresponding to the diffraction planes (111), (200), and (220), respectively (ICDD PDF 01-089-3080). We have also identified a small contribution from the diffraction of Ni (200) plane.

Room temperature Raman spectra of the composite material, as well as a reference sample collected from the carbon graphite anode, are shown in Figure 4. In the low wavenumber region, Figure 4(a) shows the typical Raman modes of NiO. A clear peak appears at 554 cm^{-1} corresponding to the one-phonon longitudinal optical (LO) mode, preceded by a transverse mode (TO) mode represented by a small hump at $400\text{--}410 \text{ cm}^{-1}$. The two-phonon

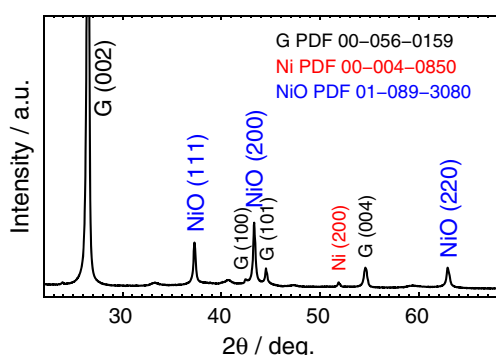


Figure 3. Powder X-ray diffraction patterns of composite NiO/graphitic flakes material.

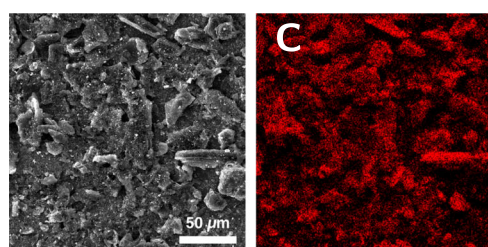


Figure 2. Scanning electron micrograph and corresponding C, Ni, and O two-dimensional energy-dispersive X-ray spectrometry of composite NiO/graphitic flakes material.

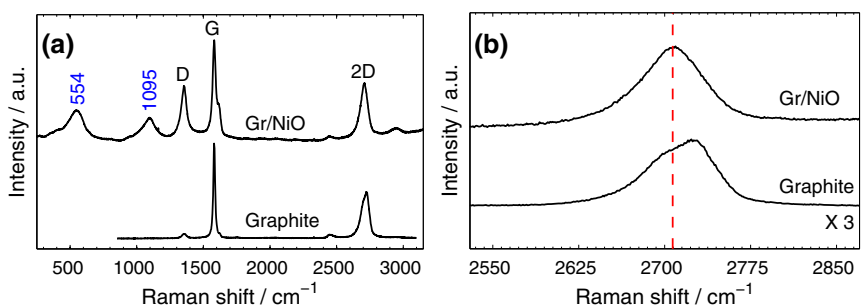


Figure 4. (a) Raman spectra of composite NiO/graphitic flakes material with carbon graphite as reference and (b) zoomed portion of Raman spectra around the 2D peak.

2LO mode of NiO is detected at 1095 cm⁻¹ [37]. At higher wavenumbers, the first-order Raman active mode of graphite, denoted by *G* and originating from the doubly degenerate (TO and LO) in-plane optical phonon mode, is observed at 1582 cm⁻¹ for our sample, and at 1581 cm⁻¹ for the graphite reference [38,39]. The disorder-induced *D* peak is observed at 1356 cm⁻¹ with much higher intensity in our sample versus pristine graphite. The intensity ratio of the *D* peak to the *G* peak (I_D/I_G) is 0.52 for our sample versus 0.03 for the carbon graphite anode material, which is an indication of increased defects in the exfoliated carbon material. Additional disorder-related responses, that is, *D'* shoulder and (*D*+*G*) peak, are observed at 1614 and 2947 cm⁻¹, respectively [40,41]. The disorder of carbon material constituting our sample may be due to oxygen functional groups at the edges of the relatively small graphitic crystals introduced during the electrochemical exfoliation process [42]. The second-order Raman scattering denoted by 2D is observed for our sample as a single well-defined peak at 2707 cm⁻¹ (Figure 4(b)), approximately twice the energy of the *D* mode [38], while for the reference graphite, it consists of two components [43]. Its intensity is ca. 0.55 times the *G* peak (I_{2D}/I_G) for our sample and 0.48 for bulk graphite. Additionally, the 2D peak of the constituent carbon in our composite material is down shift when compared with graphite, with a full width at half maximum of 52 cm⁻¹, which is an indication that it is in the form of multi-layer graphene sheets [43]. However, we will keep using the term ‘graphitic carbon flakes’ in the discussion to follow, as further investigations are needed.

To evaluate the electrochemical behavior of the composite NiO/graphitic carbon structure as potential electrode materials for electrochemical energy storage applications, CV, galvanostatic charge/discharge, and EIS have been carried out using a standard three-electrode configuration in a 5 mol l⁻¹ KOH solution. Figure 5(a) shows the stabilized CV features of the electrode material at different voltage sweep rates from 100 down to 5 mV s⁻¹, over the potential window 0–0.5 V versus SCE. The current is normalized with the mass of deposited active material. The CV profiles show a pair of peaks observed during cathodic and anodic scans centered at ca. 0.46 and

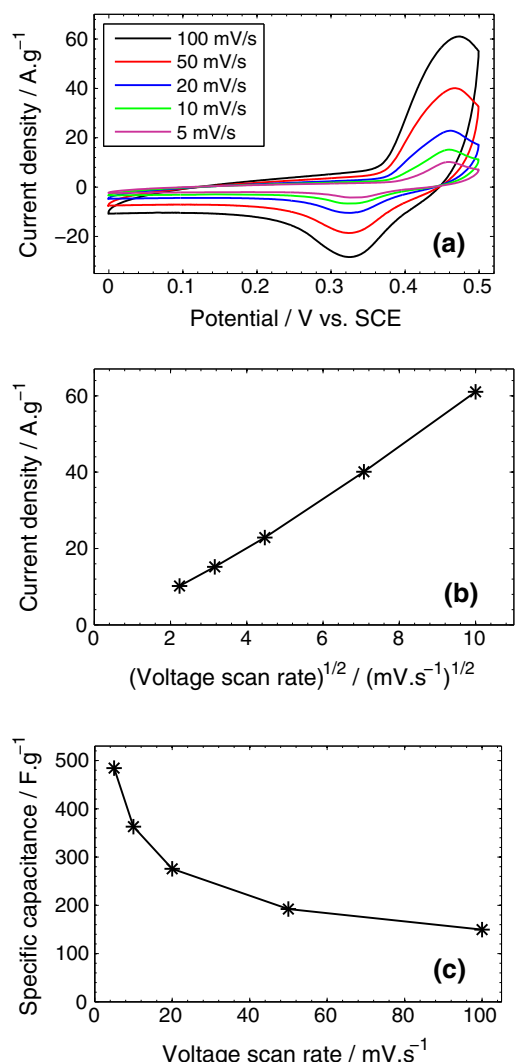


Figure 5. (a) Cyclic voltammetry over the potential window 0–0.5 V, (b) evolution of anodic current density peak with the square root of the voltage scan rate, and (c) average mass specific capacitance versus scan rate of composite NiO/graphitic flakes material in 5 mol l⁻¹ KOH solution.

0.32 V, respectively, corresponding to the reversible redox reaction:



where $0 < z < 1$ is the fraction of available sites at NiO for the insertion of OH^- ions. Additionally, with the increase of potential scan rate, the voltammograms still maintain their shape with progressive increase of anodic and cathodic current responses. From Figure 5(b), which shows the linear increase of anodic current density peak with the square root of the voltage scan rate (from Randle–Sevcik equation), we can deduct that the redox reaction at the electrode/electrolyte interface is diffusion-controlled, and therefore, the charge transfer is relatively fast. Apart from the Ni(II)/Ni(III) redox peaks, in the 0 to ca. 0.20 V potential range, the CVs show a wide separation between the positive and negative current responses, manifesting in a quasi-rectangular shape characteristic for double-layer capacitance and originating from the graphitic material. This implies that our material combines both the electric double-layer capacitive behavior of carbon and faradic response of NiO [20]. The average mass specific capacitance, calculated from the CV curves as $c = \frac{\int I(V)dV}{mv\Delta V}$, with the numerical integration of the current being over the half-cycle potential window 0–0.5 V, m the mass of the deposited material, and v the potential scan rate, is plotted in Figure 5(c) with respect to the voltage scan rate. It shows a progressive increase of the capacitance from 149 to 484 F g^{-1} with the decrease of the scan rate from 100 to 5 mV s^{-1} , which can be attributed to an enhanced diffusion

and migration of charge carriers into the active materials at lower scan rates.

Galvanostatic charge/discharge measurements of composite NiO/graphitic carbon material are conducted at the current densities of 40 down to 2 A g^{-1} , while the potential is limited to the window 0 to 0.5 V. The values of current densities are chosen to be in the same order as the peak current values in the CV curves (Figure 5(a)). Figure 6(a) shows some selected charge/discharge profiles for better readability. The charging step shows a first linear part corresponding to the oxidation of the electrode material followed by a second stage corresponding to the charging process itself. Similarly, the nonlinear discharge curves show first a quick potential drop behavior followed by a linear capacitive characteristic. The integral specific capacitance calculated as $c = \frac{I\Delta t}{m\Delta V}$, with Δt being the time required for discharging, is plotted versus the different applied current densities in Figure 6(b). It shows an inverse variation of the capacitance versus the charge/discharge rate from 27.6 F g^{-1} at the current density 40 A g^{-1} up to 495 F g^{-1} at 2 A g^{-1} , which are in close agreement with those calculated from the CV plots. These values of capacitance are higher than 309 F g^{-1} at 1 A g^{-1} reported for hierarchically porous NiO film [28], 405 F g^{-1} at 0.5 A g^{-1} for mesoporous NiO nanotubes [44], or 218 F g^{-1} at 2.7 A g^{-1} for our recent work on NiO nanoparticles synthesized with CGDE [15]. The energy density ($c\Delta V^2/2$) versus power density ($P = E/\Delta t$) calculated from the galvanostatic charge/discharge results are plotted in Figure 6(c). The Ragone plot shows a decrease of the energy density from 17.21 to 0.96 Wh kg^{-1} , as the power density increases

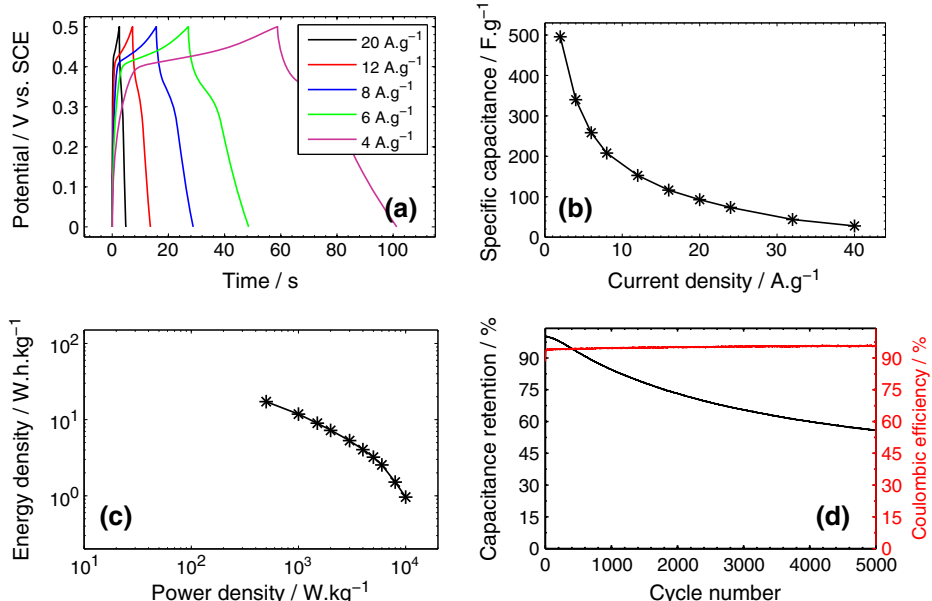


Figure 6. (a) Galvanostatic charge/discharge curves and (b) mass specific capacitance of composite NiO/graphitic flakes material vs. current density. Ragone plot (c) shows an energy density from 17.21 to 0.96 Wh kg^{-1} for a power density from 500 to $10,000 \text{ kW kg}^{-1}$. Figure (d) shows the capacitance retention of the electrode material over 5000 cycles of successive charge/discharges at 12 A g^{-1} , with over 95% coulombic efficiency.

from 500 to 10,000 W kg⁻¹. Note here that the energy–power relationship of a two-terminal device instead, consisting of NiO/graphitic structures versus an appropriate negative electrode, is more suited for better characterization [19]. We have also evaluated the long-term constant-current charge/discharge cycling stability of the electrode material. Figure 6(d) depicts both the capacitance retention and the coulombic efficiency obtained over 5000 cycles at the current density of 12 A g⁻¹. The material exhibits a reasonable stability with the capacitance steadily declining down to 56% from its initial value, which can be attributed to local structural damages and deterioration of the electrode. Similar performance was reported for composite Ni(OH)₂-thin graphite foam with capacitance retention of 65% after 1000 cycles at 10 A g⁻¹ [45]. Furthermore, the coulombic efficiency of the composite electrode materials calculated as the ratio of discharge-to-charge capacities exceeds 95% all along the 5000 cycles.

Potentiostatic EIS was used to characterize the electric properties of the electrode material. Figure 7(a) shows the Nyquist impedance plane representation of the electrode obtained at open circuit potential with 10 mV ac voltage after 50 charge/discharge cycles. The impedance plot shows globally an inclination of about -45° in the low frequency region, suggesting that the electrode is acting like a fractional capacitor with distributed resistance-capacitance behavior. An ideal capacitor would show a -90° shift between the ac voltage and ac current responses. The equivalent circuit of Randle's model, shown in the inset in Figure 7(a), was used for EIS data fitting (by complex nonlinear least-squares regression fitting routine over the whole frequency bandwidth 500 kHz to 10 mHz). It is composed of (i) an equivalent series resistance (R_s) in series with (ii) the double-layer constant phase element (CPE_{DL}), which is in parallel with a Warburg element (Z_W) and a charge-transfer resistance (R_{CT}), all in series with (iii) a parallel circuit of leakage resistance R_L and leakage CPE_L [46]. The equivalent series resistance R_s is found from the intercept of the plot with zero Im(Z) to be 1.35 Ω (Table I) at a frequency of 26 kHz, which corresponds to the electrolytic solution resistance and the internal resistance of the electrode. The charge-transfer resistance, R_{CT} , characterizes the kinetics of the faradic redox reactions Ni(II)/Ni(III) at the electrode/electrolyte

Table I. Electrochemical impedance spectroscopy fitting data for different charge/discharge cycles. The Warburg impedance Z_W can be determined from S_W using $\sqrt{2S_W/\sqrt{\omega}}$, $CPE_{DL} = 1/Q_{DL}(i\omega)^{\alpha_{DL}}$, and $CPE_L = 1/Q_L(i\omega)^{\alpha_L}$.

Cycle num.	0	50	160	5160
R_s/Ω	1.41	1.35	1.36	1.31
R_{CT}/Ω	0.897	0.766	0.470	0.414
$S_W/\Omega s^{-1/2}$	150.6	150.9	119.1	100.8
$Q_{DL}/mFs^{(\alpha_{DL}-1)}$	0.239	0.303	0.235	0.200
α_{DL}	0.93	0.90	0.94	0.97
R_L/Ω	23.7	26.5	39.1	51.5
$Q_L/mFs^{(\alpha_L-1)}$	15.9	13.6	8.1	7.2
α_L	0.78	0.75	0.73	0.72

surface (reaction 2), where low values imply fast ion transport [18]. R_{CT} is found to be as low as 0.766 Ω because of enhanced contact area of NiO materials with the electrolyte. In series with R_{CT} , we have the Warburg element, which represents the frequency-dependent ionic diffusion [5]. In addition, we have the constant phase element of the double-layer capacitance (CPE_{DL}) of the electrode/electrolyte interface, which is characterized by $Q_{DL} = 0.303 mFs^{(\alpha_{DL}-1)}$ where $\alpha_{DL}=0.90$. The parameter α can take on values between 0 (element acting as a pure resistor) and 1 (element acting as an ideal capacitor) [47]. The value of 0.90 for the parameter α_{DL} is an indication that the electrode material behaves as a pseudocapacitor, although very close to the ideal capacitance characteristic. The leakage resistance is found from the EIS fitting model to be 26.5 Ω and the pseudocapacitance CPE_L to be 13.6 mFs^(α_L-1) where $\alpha_L=0.75$. In Figure 7(b), we show the mass specific differential capacitance and phase angle shift between the input voltage and output current versus frequency. The phase angle reaches -53° at 37 Hz followed by a steady increase towards the resistor behavior in the high frequency region, where the phase shift approaches zero. This confirms the distributed charge storage mechanism and pseudocapacitive behavior deducted from the inclination of the real and imaginary parts of the impedance, as shown in Figure 7(a). From the variation of the mass specific differential capacitance, we note that the electrode material exhibits a capacitive behavior maintained over a wide

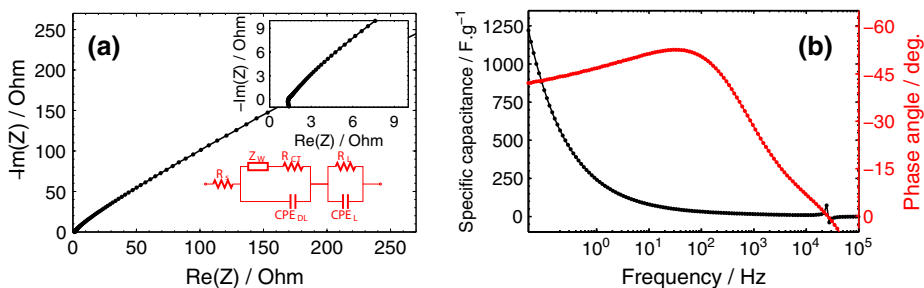


Figure 7. (a) Nyquist impedance representation and (b) Bode diagram showing the specific capacitance-frequency and phase-frequency plots of composite NiO/graphitic flakes material over the frequency range 500 kHz to 10 mHz.

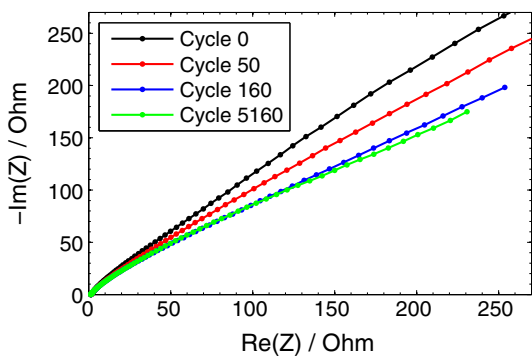


Figure 8. Nyquist plot for impedance plane representation measured at different charge/discharge cycles.

frequency domain close to the dc limit. Note that the discontinuity observed at high frequency, where the imaginary part of the impedance passes through zero (phase angle shift turns positive), is just an artifact of the instrument.

To evaluate the change of the electric behavior of the electrode material with the charging/discharging process, we have conducted the EIS measurements at multiple intervals, that is, for the freshly prepared electrode (Cycle 0), as well as after 50, 160, and 5160 charge/discharge cycles, as shown in the Nyquist plots in Figure 8. The corresponding EIS fitting data using the same electric model shown in Figure 7(a) are summarized in Table I. The equivalent series resistance R_s decreased from $1.41\ \Omega$ for the freshly prepared electrode to $1.31\ \Omega$ by the end of the 5160th. This is most probably due to enhanced electrolyte penetration and ion diffusion into the electrode material by the series of cyclic charges/discharges. The same observation holds for the decreasing value of R_{CT} , which is associated with more active reaction sites at the electrode surface, with the increase of cycle number [18]. The CPE_{DL} value is slightly decreased by the end of the 5160th cycle, probably due to some local agglomeration of the electrode materials. The parameter α_{DL} is always above 0.90, which confirms the double-layer ideal capacitance behavior in this region. In contrast, the leakage resistance shows an increasing trend from cycle 0 to cycle 5160, which can be attributed to a delamination of the deposited materials due to the formation of some electrolyte pockets. Finally, the characteristic impedance of CPE_L represented by Q_L and α_L is reduced by 45% from its initial value, which is in line with long-term cyclability results obtained in Figure 6(d). CPE_L is at least one order of magnitude larger than CPE_{DL}.

4. CONCLUSION

In summary, we demonstrated a simple one-pot procedure for the preparation of composite graphitic flakes with NiO material using cathodic CGDE for supercapacitor application. The electric discharges generated at 120 Vdc within the micro-plasma volume around the Pt wire progressively reduce Ni²⁺ precursors into NiO, whereas the carbon anode

is exfoliated by ion/solvent intercalation. The structured material exhibits a high mass specific capacitance reaching $495\ \text{F g}^{-1}$ at $2\ \text{A g}^{-1}$ current density. With 5000 successive cycles of charges/discharges at $12\ \text{A g}^{-1}$, the electrode maintained over 55% of its original capacitance with a coulombic efficiency exceeding 95%. Additionally, we showed from the EIS measurements that the composite graphitic carbon flakes-supported NiO material exhibits a pseudocapacitive behavior over a wide range of frequency while maintaining an overall considerable electric response.

ACKNOWLEDGEMENTS

This work was supported by the University of Sharjah (project no. 140232). We would like to acknowledge the assistance of M. Shameer and H. Bilal, as well as the X-ray Center for Material Analysis.

REFERENCES

1. Srithorn P, Sumner M, Yao L, Parashar R. Power system stabilisation using STATCOM with supercapacitors, in: Industry Applications Society Annual Meeting, 2008. IAS '08. IEEE, 2008; 1–8.
2. Wu B, Parkes MA, Yufit V, Benedetti LD, Veismann S, Wirsching C, Vesper F, Martinez-Botas RF, Marquis AJ, Offer GJ, Brandon NP. Design and testing of a 9.5 kWe proton exchange membrane fuel cell-supercapacitor passive hybrid system. *International Journal of Hydrogen Energy* 2014a; **39**(15): 7885–7896.
3. Conway B, Birss V, Wojtowicz J. The role and utilization of pseudocapacitance for energy storage by supercapacitors. *Journal of Power Sources* 1997; **66**(1-2):1–14.
4. Simon P, Gogotsi Y. Materials for electrochemical capacitors. *Nature Materials* 2008; **7**(11):845–854.
5. Kötz R, Carlen M. Principles and applications of electrochemical capacitors. *Electrochimica Acta* 2000; **45**(15–16):2483–2498.
6. Burke A. Ultracapacitors: why, how, and where is the technology. *Journal of Power Sources* 2000; **91**(1):37–50.
7. An KH, Kim WS, Park YS, Moon J-M, Bae DJ, Lim SC, Lee YS, Lee YH. Electrochemical properties of high-power supercapacitors using single-walled carbon nanotube electrodes. *Advanced Functional Materials* 2001; **11**(5):387–392.
8. El-Kady MF, Strong V, Dubin S, Kaner RB. Laser scribing of high-performance and flexible graphene-based electrochemical capacitors. *Science* 2012; **335**(6074):1326–1330.

9. Arbizzani C, Mastragostino M, Meneghelli L. Polymer-based redox supercapacitors: a comparative study. *Electrochimica Acta* 1996; **41**(1):21–26.
10. Laforgue A, Simon P, Sarrazin C, Fauvarque J-F. Polythiophene-based supercapacitors. *Journal of Power Sources* 1999; **80**(1–2):142–148.
11. Mastragostino M, Arbizzani C, Soavi F. Polymer-based supercapacitors. *Journal of Power Sources* 2001; **97–98**:812–815.
12. Snook GA, Kao P, Best AS. Conducting-polymer-based supercapacitor devices and electrodes. *Journal of Power Sources* 2011; **196**(1):1–12.
13. Jiang J, Li Y, Liu J, Huang X, Yuan C, Lou XWD. Recent advances in metal oxide-based electrode architecture design for electrochemical energy storage. *Advanced Materials* 2012; **24**(38):5166–5180.
14. Wang H, Casalongue HS, Liang Y, Dai H. Ni(OH)₂ nanoplates grown on graphene as advanced electrochemical pseudocapacitor materials. *Journal of the American Chemical Society* 2010; **132**(21):7472–7477.
15. Allagui A, Alami AH, Baranova EA, Wüthrich R. Size-dependent capacitance of nickel oxide nanoparticles synthesized with contact glow discharge electrolysis. *Journal of Power Sources* 2014; **262**:178–182.
16. Yu G, Hu L, Vosgueritchian M, Wang H, Xie X, McDonough JR, Cui X, Cui Y, Bao Z. Solution-processed graphene/MnO₂ nanostructured textiles for high-performance electrochemical capacitors. *Nano Letters* 2011; **11**(7):2905–2911.
17. Liu TC, Pell WG, Conway BE. Stages in the development of thick cobalt oxide films exhibiting reversible redox behavior and pseudocapacitance. *Electrochimica Acta* 1999; **44**:2829–2842.
18. Wang W, Guo S, Lee I, Ahmed K, Zhong J, Favors Z, Zaera F, Ozkan M, Ozkan CS. Hydrous ruthenium oxide nanoparticles anchored to graphene and carbon nanotube hybrid foam for supercapacitors, *Scientific Reports* 4: 4452. DOI: 10.1038/srep04452
19. Allagui A, Salameh T, Alawadhi H. Dendritic CuO structures synthesized by bipolar electrochemical process for electrochemical energy storage. *Journal of Electroanalytical Chemistry* 2015a; **750**:107–113.
20. Yang Z-C, Tang C-H, Zhang Y, Gong H, Li X, Wang J. Cobalt monoxide-doped porous graphitic carbon microspheres for supercapacitor application, *Scientific Reports* 3: 2925. DOI: 10.1038/srep02925
21. Wu Z, Huang X-L, Wang Z-L, Xu J-J, Wang H-G, Zhang X-B. Electrostatic induced stretch growth of homogeneous β -Ni(OH)₂ on graphene with enhanced high-rate cycling for supercapacitors, *Scientific Reports* 4: 3669. DOI: 10.1038/srep03669
22. Weber C, Lorrmann V, Reichenauer G, Pflaum J. Structural and electrochemical properties of MnO₂-Carbon based supercapacitor electrodes, arXiv:1411.6278.
23. Huang Y, Huang X-l, Lian J-s, Xu D, Wang L-m, Zhang X-b. Self-assembly of ultrathin porous NiO nanosheets/graphene hierarchical structure for high-capacity and high-rate lithium storage. *Journal of Materials Chemistry* 2012; **22**:2844–2847.
24. Singh AK, Sarkar D, Khan GG, Mandal K. Hydrogenated NiO nanoblock architecture for high performance pseudocapacitor. *ACS Applied Materials & Interfaces* 2014; **6**(7):4684–4692.
25. Lee JW, Ahn T, Kim JH, Ko JM, Kim J-D. Nanosheets based mesoporous NiO microspherical structures via facile and template-free method for high performance supercapacitors. *Electrochimica Acta* 2011; **56**(13):4849–4857.
26. Wu C, Deng S, Wang H, Sun Y, Liu J, Yan H. Preparation of novel three-dimensional NiO/ultrathin derived graphene hybrid for supercapacitor applications. *ACS Applied Materials & Interfaces* 2014c; **6**(2):1106–1112.
27. Dam DT, Wang X, Lee J-M. Graphene/NiO nanowires: controllable one-pot synthesis and enhanced pseudocapacitive behavior. *ACS Applied Materials & Interfaces* 2014; **6**(11):8246–8256.
28. Xia X-h, Tu J-p, Wang X-l, Gu C-d, Zhao X-b. Hierarchically porous NiO film grown by chemical bath deposition via a colloidal crystal template as an electrochemical pseudocapacitor material. *Journal of Materials Chemistry* 2011; **21**:671–679.
29. Saha S, Ganguly S, Banerjee D, Kargupta K. Novel bimetallic graphene–cobalt–nickel (G–Co–Ni) nanoensemble electrocatalyst for enhanced borohydride oxidation. *International Journal of Hydrogen Energy* 2015; **40**(4):1760–1773.
30. Allagui A, Baranova EA, Wüthrich R. Synthesis of Ni and Pt nanomaterials by cathodic contact glow discharge electrolysis in acidic and alkaline media. *Electrochimica Acta* 2013; **93**:137–142.
31. Wüthrich R, Allagui A. Building micro and nanosystems with electrochemical discharges. *Electrochimica Acta* 2010; **55**(27):8189–8196.
32. Allagui A, Wüthrich R. Gas film formation time and gas film life time during electrochemical discharge phenomenon. *Electrochimica Acta* 2009; **54**(23):5336–5343.
33. Allagui A, Brazeau N, Alawadhi H, Almomani F, Baranova EA. Cathodic contact glow discharge electrolysis for the degradation of liquid ammonia solutions. *Plasma Processes and Polymers* 2015; **12**: 25–31.
34. Allagui A, Wüthrich R. The electrochemical discharges for the synthesis of nickel oxide nanoparticles:

- characterization and mechanism. *Electrochimica Acta* 2011; **58**:12–18.
- 35. Parvez K, Wu Z-S, Li R, Liu X, Graf R, Feng X, Müllen K. Exfoliation of graphite into graphene in aqueous solutions of inorganic salts. *Journal of the American Chemical Society* 2014; **136**(16):6083–6091.
 - 36. Lu J, Yang J-x, Wang J, Lim A, Wang S, Loh KP. One-pot synthesis of fluorescent carbon nanoribbons, nanoparticles, and graphene by the exfoliation of graphite in ionic liquids. *ACS Nano* 2009; **3**(8):2367–2375.
 - 37. Dietz RE, Parisot GI, Meixner AE. Infrared absorption and Raman scattering by two-magnon processes in NiO. *Physical Review B* 1971; **4**:2302–2310.
 - 38. Reich S, Thomsen C. Raman spectroscopy of graphite. *Philosophical Transactions of the Royal Society of London, Series A: Mathematical, Physical and Engineering Sciences* 2004; **362**(1824):2271–2288.
 - 39. Robertson J. Diamond-like amorphous carbon. *Materials Science and Engineering Reports* 2002; **37**(4):129–281.
 - 40. Hong J, Park MK, Lee EJ, Lee D, Hwang DS, Ryu S. Origin of New broad Raman D and G peaks in annealed graphene, *Scientific Reports* 3: 2700. DOI: 10.1038/srep02700
 - 41. Shen Y, Lua AC. A facile method for the large-scale continuous synthesis of graphene sheets using a novel catalyst, *Scientific Reports* 3: 3037. DOI: 10.1038/srep03037
 - 42. Rao KS, Senthilnathan J, Liu Y-F, Yoshimura M. Role of peroxide ions in formation of graphene nanosheets by electrochemical exfoliation of graphite, *Scientific Reports* 4: 4237. DOI: 10.1038/srep04237
 - 43. Ferrari AC, Meyer JC, Scardaci V, Casiraghi C, Lazzeri M, Mauri F, Piscanec S, Jiang D, Novoselov KS, Roth S, Geim AK. Raman spectrum of graphene and graphene layers. *Physical Review Letters* 2006; **97**:187401.
 - 44. Xiong S, Yuan C, Zhang X, Qian Y. Mesoporous NiO with various hierarchical nanostructures by quasi-nanotubes/nanowires/nanorods self-assembly: controllable preparation and application in supercapacitors. *CrystEngComm* 2011; **13**:626–632.
 - 45. Ji J, Zhang LL, Ji H, Li Y, Zhao X, Bai X, Fan X, Zhang F, Ruoff RS. Nanoporous Ni(OH)₂ thin film on 3D ultrathin-graphite foam for asymmetric supercapacitor. *ACS Nano* 2013; **7**(7):6237–6243.
 - 46. Hastak R, Sivaraman P, Potphode D, Shashidhara K, Samui A. All solid supercapacitor based on activated carbon and poly [2,5-benzimidazole] for high temperature application. *Electrochimica Acta* 2012; **59**:296–303.
 - 47. Freeborn T, Maundy B, Elwakil A. Measurement of supercapacitor fractional-order model parameters from voltage-excited step response. *IEEE Journal on Emerging and Selected Topics in Circuits and Systems* 2013; **3**(3):367–376.